Synthesis, Optical Absorption, and Site-Selective Excitation of the $^3P_0$ Levels in $Y_4Al_2O_9:Pr^{3+}$

Y. Rabinovitch,[†] O. K. Moune,[‡] D. Tétard,[†] and M. D. Faucher*[,§]

Science des Procédés Céramiques et de Traitements de Surface, UMR 6638, Faculté des Sciences de Limoges, 123 Avenue Albert Thomas, 87060 Limoges Cedex, France, Structure, Propriétés et Modélisation des Solides, UMR 8580, Ecole Centrale Paris, 92295 Châtenay-Malabry Cedex, France, and 88 Avenue Jean Jaurès, 92140 Clamart, France

Received: April 30, 2004; In Final Form: July 7, 2004

$Y_4Al_2O_9:Pr^{3+}$ was prepared by two methods: starting from the citrates and direct sintering of the oxides. The latter method gave more single-phased samples. Optical spectroscopy was utilized to obtain the emission spectra from the individual sites of the crystal structure. Absorption, excitation spectra, and site-selective excitation into the $^3P_0$ levels were utilized. Only three sites out of four were detected, and their energy levels were singled out. The crystal-field parameters of each set were determined, and an attempt was made to correlate optical spectra and crystallographic sites.

Introduction

Early phase diagrams of the $Re_2O_3-Al_2O_3$ (Re = rare earth,Y) system[1] revealed the presence of the garnet $Re_3Al_5O_{12}$, the perovskite $ReAlO_3$ (YAP), and the compound $Re_4Al_2O_9$ (YAM), with Re/Al ratios equal to 0.6/1, 1/1, and 2/1, respectively. The latter was first obtained for the smaller rare-earth elements for Re = Gd−Yb (and Y). Brandle and Steinfink[2] prepared the compound for Re = Sm, Eu, and Lu and solved the structure of $Eu_4Al_2O_9$ on a single crystal. It was subsequently shown that $Nd_4Al_2O_9$,[3] $La_4Al_2O_9$, $Pr_4Al_2O_9$, and $Tb_4Al_2O_9$[4] could be prepared as well. The compounds are isostructural from Re = Sm−Lu. The structure is monoclinic with space group $P2_1/c$ (No. 14). Structure refinements of the $Y_4Al_2O_9$ structure from powder, X-ray, and neutron diffraction data on a single crystal have been more recently reported.[5] The room-temperature phase of $Y_4Al_2O_9$ can therefore be considered as precisely defined. A high-temperature phase transition at 1370 °C was detected on a sintered polycrystalline sample of $Gd_4Al_2O_9$,[6] the space group of the high-temperature phase being $P2_1/c$, the same as that for the low-temperature phase. The high-temperature phase is partially stabilized by small additions of MgO.[7a] A further monoclinic to orthorhombic phase transition occurs at 1700 °C.[7b] There are four formula units in the unit cell of the room-temperature phase of $Y_4Al_2O_9$ and four different rare-earth sites in the asymmetric unit. Spectroscopic investigations on this compound doped with lanthanide ions have been sparse,[3,8] and none of them concern Pr^{3+}. After a previous spectroscopic study of $Y_3Al_5O_{12}:Pr^{3+}$,[9] the goal of the present work is an investigation of the optical properties of a Pr^{3+}-doped $Y_4Al_2O_9$ sample. It will be determined whether the results obtained by site-selective spectroscopy agree with the conclusions of the X-ray studies. After describing the preparation of the compounds and the characteristics of the samples, we shall give an account of the spectroscopic studies, namely the absorption and emission under site-selective excitation and the crystal-field determination. The last part will be an attempt to identify the observed spectra with the crystallographic sites.

Preparation and Characterization of the Samples

The literature reports several methods for preparing $Re_4Al_2O_9$: first, by high-temperature, solid-state techniques starting from stoichiometric mixtures of the oxides. Samples may be prepared by any of the following techniques: (a) melting on a water-cooled copper hearth under an argon atmosphere;[2,3] (b) pressing isostatically to a rod, heating at 1340 °C for 24 h, and then melting in a crystal furnace;[5] (c) placing in an iridium crucible and melting in an induction furnace. The resulting crystal is brittle and breaks upon cooling.[10] An additional technique would be (d) sintering between 1273 and 1973 K.[11] More recently, alternative methods have been worked out to allow processing at a lower temperature. For instance, $Re_4Al_2O_9$ (Re = La, Pr, Tb) was prepared by the precipitation of the rare-earth nitrate by aluminum hydroxide followed by firing at 900 °C.[4] Other authors prefer preparations relying on "chimie douce"[12] or sol−gel[8,13] methods.

In the present work, both a chimie douce route and the mixed-oxides method were utilized for the preparation of $Y_4Al_2O_9:Pr^{3+}$. One sample hereafter designated by Ci was synthesized by the chimie douce route starting from the citrates. A mixture of yttrium, praseodymium, and aluminum nitrates and citric acid was slowly evaporated at 140−150 °C, and then heated to 200 °C on a hot plate. The dry residue was then placed in an air furnace where it was decomposed at 650 °C for 12 h to eliminate carbon residues. It was then pressed and sintered above 1700 °C in a vacuum furnace as in the mixed-oxides method, which will be described.

The preparation by the mixed-oxides method is similar to that used previously for $YAG:Pr^{3+}$ [9] and $YAG:Nd^{3+}$.[14,15] Commercial oxides are utilized: alumina and yttrium oxide, 99.99% from Alfa Aesar, the mean grain dimensions being 100 and 800 nm, respectively; praseodymium oxide (REacton 99.99%) with a grain dimension of 6 μm. The powders are

* Corresponding author. E-mail: faucher.michele@free.fr.
[†] Science des Procédés Céramiques et de Traitements de Surface, Faculté des Sciences de Limoges. E-mail: yr@levillage.org.
[‡] Structure, Propriétés et Modélisation des Solides, Ecole Centrale Paris. E-mail: moune@spms.ecp.fr.
[§] 88 Avenue Jean Jaurès, 92140 Clamart, France.

10.1021/jp048123j CCC: $27.50
Published on Web 09/09/2004

TABLE 1: Sintering Conditions and Characteristics of the Samples[a]

sample % Pr^{3+}	T^b °C	DT	CR	XRD YAM +	ABS 20 K YAM + $^3P_0$	$^3P_1$, $^1I_6$?	$^1D_2$	$^3F_3$	$\Delta\sigma1$	$\Delta\sigma2$
0.1	1780	3	10	YAP						
0.1 + SiO_2	1780	3	10	YAP						
0.1[c] Ci				YAP?	YAP?	YAP	YAP + ?		~33	13.2
1	1780	3	10	YAP	YAP	YAP	YAP^{vvS}		22	21
1 + SiO_2	1780	3	10	YAP						
(0.5) **I**	1780	3	10	YAP?	YAP	YAP	YAP^{vS}		17.6	13.2
(0.5) **II**	1780	3	20	YAP	YAP	YAP	YAP^{S}		13.2	16.5
(0.5) **III**	1780	1	20	YAP?	YAP	YAP	YAP^{S}	YAP^{vS}	13.2	11
(0.5) **IV**[d]	1800	1	20	YAP?	YAP?	YAP	YAP^{S}	YAP^{S}	7.7	8.8
(0.5) **V**	1750	1	20				YAP^{W}	YAP^{M}	17.6	17.6
(0.5) **VI**	1700	1	20				YAP^{W}	YAP^{W}	22	21

[a] DT = dwell time (h); CR = cooling ramp (°C/min); $\Delta\sigma1$, $\Delta\sigma2$ = width (cm^{-1}) at half-height of the $^3H_4 \rightarrow {}^3P_0$ lines at 20 530 and 20 764 cm^{-1}, respectively; W = weak; M = medium; S = strong; vS = very strong; vvS = very, very strong. [b] Heating ramp = 10 °C/min). [c] Chimie douce (citrate) route. [d] One side of the sample was molten and stuck to the alumina crucible. The data refer to the other (intact) side.

weighed in order to produce the sample $Pr_xY_{1-x}Al_5O_{12}$. A portion of 1% silica (Alfa Aesar 99.8%) is eventually added as a sintering aid. The powders are stirred in alcohol with yttria-stabilized zirconia balls for 24 h in a roll-on bottle. Still damp, they are pressed hydrostatically at 300 MPa to small disks about 12 mm in diameter and 1.3 mm thick. The samples, embedded in a powder of the same composition, are placed in an alumina crucible. They are finally heated at temperatures ranging from 1700 to 1800 °C under vacuum (10^{-3} Pa). Processing under vacuum reduces the porosity and prevents Pr^{3+} from oxidizing into Pr^{4+}.

Sample Characterization: X-ray Diffraction and Optical Absorption Spectra

The phases present in the samples were checked by combining X-ray diffraction analyses and optical absorption spectroscopy and comparing with known spectra. The samples were placed in a He closed-cycle cryostat (model CP-62-ST/5 from Cryophysics). The temperature was estimated at 20 K. The absorption spectra in the region from 4000 to 22 000 cm^{-1} were recorded on a CARY 5E spectrometer.

Table 1 summarizes the sintering conditions and the sample characteristics. In column 1, the Pr^{3+} atomic content is reported: 0.1, 0.5, or 1 atom %. The presence of SiO_2 is eventually noted. In columns 2, 3, and 4 are listed the sintering temperature, the dwell time, and the cooling ramp, respectively. The temperature ranges from 1700 to 1800 °C, lower than the 1835 °C eutectic which is present between the compositions $2Y_2O_3-Al_2O_3$ and $3Y_2O_3-5Al_2O_3$. The dwell time ranges between 1 and 3 h, and the cooling ramp is 10 or 20 °C/min. This rather rapid cooling seems advisable according to the conclusions of previous studies.[2,3] Column 5 in Table 1 lists the main phase impurities observed in the X-ray diffraction patterns, and columns 6−9 list those detected in the optical absorption spectrum.

Concerning the doping concentration, 0.1 atom % was introduced at first, but the signal emitted by Pr^{3+} was too weak to obtain a good-quality emission spectrum. This can be understood, because the Pr^{3+} amount is to be shared by four crystallographic sites. Next, 1 atom % Pr^{3+}, a quantity 10 times larger, was doped into the sample. Characteristic lines of YAP ($YAlO_3$) are then present in the XRD pattern as well as strong absorption lines in the $^3H_4 \rightarrow {}^3P_0$, $^3P_1$, $^1I_6$, and $^3H_4 \rightarrow {}^1D_2$ spectral areas, with $^3H_4 \rightarrow {}^1D_2$ as the main absorption area.[16] An intermediate doping concentration (0.5 atom % Pr^{3+}) permitted us to obtain more single-phased samples, along with acceptable optical signals. It was considered a good compromise and was adopted for samples I−VI.

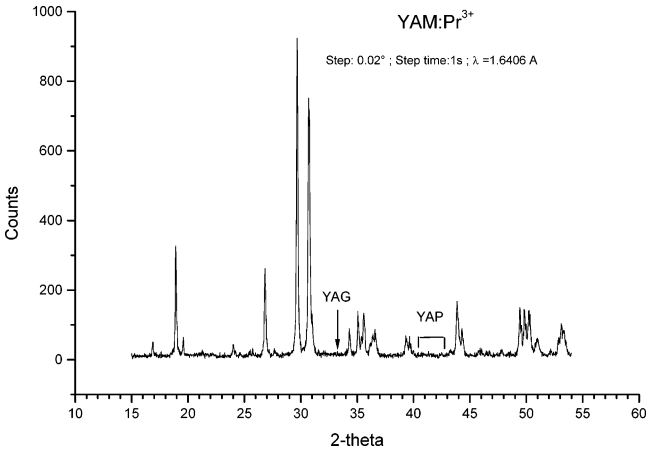

Figure 1. Room-temperature X-ray diffraction pattern of $Y_4Al_2O_9:Pr^{3+}$ 0.5% heated for 1 h at 1700 °C (sample VI). Void zones are indicated, where YAG:Pr^{3+} and YAP:Pr^{3+} lines can be best detected.

The diffraction lines of YAP are present in the XRD diagrams of the sample with 0.1% Pr and 1% silica but not in samples V and VI. Figure 1 shows the diffraction pattern of sample VI, devoid of spurious YAG and YAP lines. Optical absorption is more sensitive for the detection of impurities, and the perovskite was detected in nearly all of the spectra. Figure 2a compares the $^3H_4 \rightarrow {}^1D_2$ absorption of samples Ci and VI in the 16 000−18 000 cm^{-1} spectral area (the absorbance of the Ci sample is multiplied by 10). Absorption lines of YAP:Pr[16] appear in the Ci spectrum at 16 380 (weakly), 16 717, and 17 031 cm^{-1} (on the right shoulder of the line at 17 023 cm^{-1}). However, the prohibitive feature of sample Ci consists of an unidentified impurity causing a strong massif of unassigned lines occupying the middle of the spectrum between 16 766 and 17 023 cm^{-1} and 17 120 and 17 438 cm^{-1}. We were able to classify these as impurity lines only after analyzing more single-phased samples (samples IV and VI). Their presence was the reason for abandoning the citrate preparation mode in favor of direct sintering of the oxides.

The best samples were translucent, yet never as transparent as the previously obtained YAG:Nd^{3+} [14,15] or (to a lesser extent) YAG:Pr^{3+}.[9] For instance, the optical densities per millimeter of samples I, II, and III in the $^3H_4 \rightarrow {}^1D_2$ and $^3H_4 \rightarrow {}^3P_0$ spectral ranges are equal to 3.3, 2.7, and 2.4, respectively, whereas that of YAG:Pr^{3+} was on the order of 1.0[9] and that of YAG:Nd^{3+} was 0.083.[14] The reasons are as follows: The melting points of the garnet $Y_3Al_5O_{12}$ (YAG:3/5), the perovskite $YAlO_3$ (YAP: 1/1), and $Y_4Al_2O_9$ (YAM:2/1) are equal to 1930, 1875, and 2020

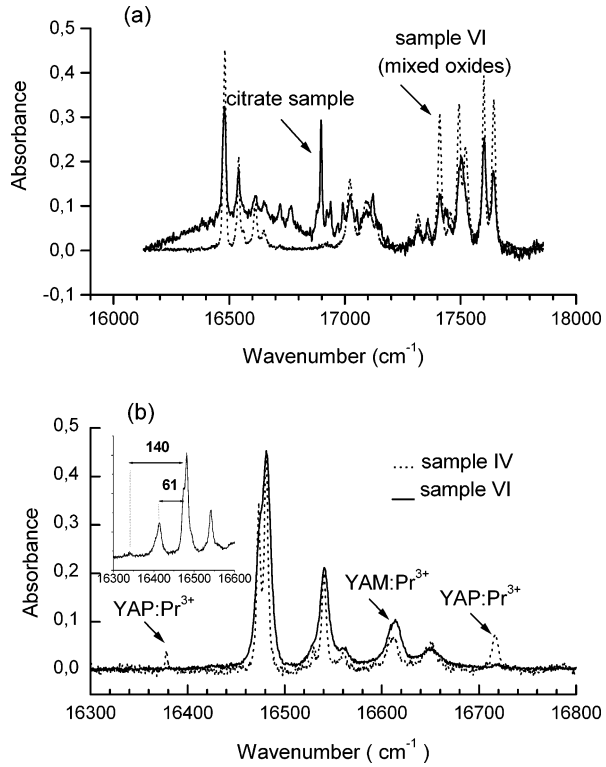

Figure 2. (a) $^3H_4 \rightarrow {}^1D_2$ absorption spectra at 20 K of samples citrate (Ci) and VI in the 16 000−18 000 cm^{-1} spectral area. The absorbance of the Ci sample is multiplied by 10. The samples are described in Table 1. (b) $^3H_4 \rightarrow {}^1D_2$ absorption spectra of samples IV and VI in the 16 300−18 000 cm^{-1} spectral area. The insert represents a part of the 90 K spectrum in which two hot lines are shown.

°C, respectively.[17] The lowest melting point is that of YAP, which is the most easily formed. Also, the Goldschmidt tolerance factor[18] evaluated with the ionic radii of Pr^{3+} and Al^{3+} is in favor of the perovskite. As a consequence of these facts, the preferred phase in the $Pr_2O_3-Al_2O_3$ system is YAP($PrAlO_3$). Thus, Pr^{3+}, a larger ion than Y^{3+}, is likely to induce in the host matrix the formation of small domains with the perovskite structure. These domains are defects, which detract from the transparency of the sample.

One face of sample IV that was heated for 1 h at 1800 °C melted on contact with the alumina crucible, because a eutectic at 1750 °C exists in the alumina-rich part of the $Y_2O_3-Al_2O_3$ system.[17] The other face would be acceptable except for the presence of some YAP impurity lines in the optical absorption spectrum, while the XRD pattern hardly showed any. Sample IV displays the narrowest spectral lines yet.

The purest sample is sample VI, heated for 1 h only at 1700 °C. Figure 2b compares the $^3H_4 \rightarrow {}^1D_2$ absorption of samples IV and VI in the 16 300−18 000 cm^{-1} spectral area. Two YAP:Pr^{3+} lines at 16 380 and 16 717 cm^{-1} are present in the spectrum of IV; they are hardly visible in sample VI.

The number of crystallographic Pr^{3+} sites present in a structure can, in principle, be deduced from the number of lines in the $^3H_4 \rightarrow {}^3P_0$ spectral range. Still, the interpretations may be erroneous because of the presence of $^3H_4 \rightarrow {}^1I_6$ transitions in that area and/or the accidental coincidence of spectral lines. Figure 3 shows the optical absorption spectrum of samples IV and VI in the 20 500−20 900 cm^{-1} zone. It is not probable that the $^3H_4 \rightarrow {}^3P_0$ transitions lie outside that zone. Sample IV gives rise to sharper lines, but otherwise, the two spectra are similar: Five lines are recorded at 20 530, 20 671, 20 726, 20 762, and 20 823 cm^{-1}. Their relative strengths are approximately the same

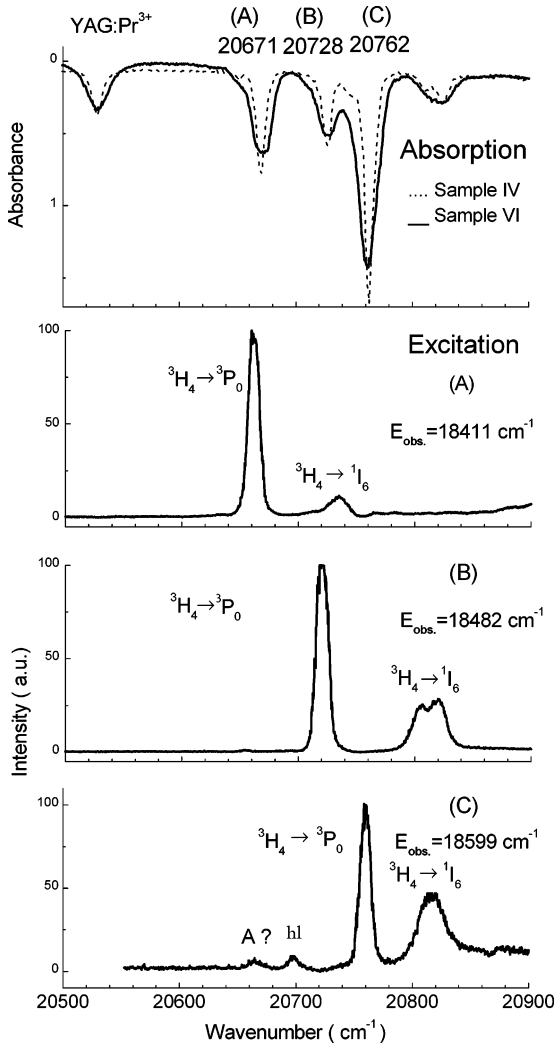

Figure 3. Optical absorption spectra at 20 K of samples IV and VI in the 20 500−20 900 cm^{-1} zone. Excitation spectra of sites A, B, and C in sample VI.

in the two spectra. The first one at 20 530 cm^{-1} occurs at the same energy as the $^3H_4 \rightarrow {}^3P_0$ absorption of YAG:Pr^{3+} (measured at 20 536 cm^{-1}).[9] Upon selective excitation at 20 530 cm^{-1}, one YAG $^3P_0 \rightarrow {}^3H_4$ line is present among other unidentified lines in a weak, ill-defined spectrum. Columns 10−11 of Table 1 record the width (cm^{-1}) at half-height of the lines at 20 530 and 20 764 cm^{-1}. The former is quite broad in the citrate sample, which hints to a different origin. The feature at 20 530 cm^{-1} is therefore ascribed to YAG. It is observed in that area only because the $^3H_4 \rightarrow {}^3P_0$ transitions of YAG:Pr^{3+} are about 14 times stronger than the $^3H_4 \rightarrow {}^1D_2$ transitions, while the ratio is only equal to 3 for YAM:Pr^{3+}. Further investigation is necessary to determine which of the four remaining lines are to be ascribed to the YAM:Pr^{3+} $^3H_4 \rightarrow {}^3P_0$ transitions.

The width of the line at 20 764 cm^{-1} is less than 10 cm^{-1} for sample IV and 2 and 2.5 times larger for samples V and VI, respectively (Table 1). Yet, we have retained sample VI, the purest according to Table 1, for most of the subsequent emission investigations. Purity seems to be the main criteria for the selection of a sample because of the quasi-unavoidable and overwhelming presence of YAP. Besides, site-selective excitation of the optical emission allows the production of good-quality spectra by a narrowing of the spectral lines. Figure 4 presents the absorption spectrum in the $^3H_4 \rightarrow {}^3H_6$, $^3F_2$ and $^3H_4 \rightarrow {}^3F_{3-4}$ ranges. In a multisite compound, time-resolved

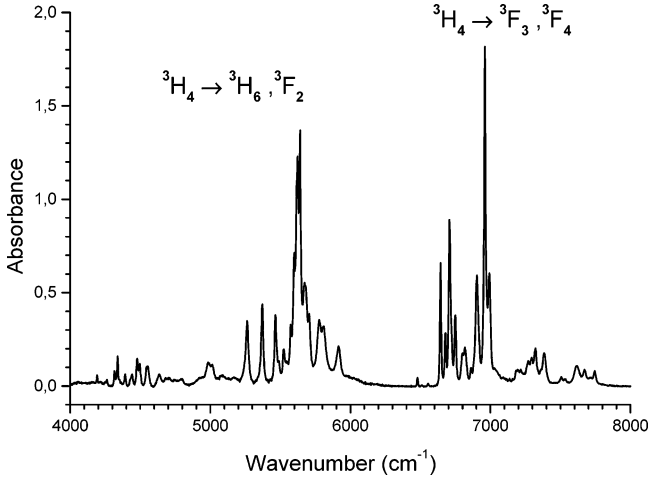

Figure 4. Absorption spectrum at 20 K of sample VI in the $^3H_4 \rightarrow {}^3H_6$, $^3F_2$ and $^3H_4 \rightarrow {}^3F_{3-4}$ spectral areas.

emission and excitation spectra are necessary to differentiate the spectra belonging to each different site.

Experimental Setup

The site-selective emission and excitation spectra in the 430−860 nm spectral region were obtained by means of an optical parametric oscillator (Quanta-Ray MOPO-730) pumped by the third harmonic at 355 nm (8 ns pulse at 10 Hz, 0.1 cm^{-1} width) of a Q-switched neodymium YAG laser (GCR-230) from Spectra-Physics. The spectra were recorded using a double-grating spectrometer (model PHO from Coderg) equipped with an R928 Hamamatsu photomultiplier. Time-resolved fluorescence and fluorescence lifetime were measured via a digital oscilloscope (Tektronix 2430) coupled with a microcomputer. The experimental setup is described elsewhere.[19]

Site Selection: Excitation Spectra

Direct excitation at 355 nm by the pump laser displayed no exploitable emissions in the $^3P_0-{}^3P_1-{}^1I_6 \rightarrow {}^3H_4$ region. The first step consisted of determining which of the four lines observed in the absorption spectrum between 20 600 and 20 900 cm^{-1} could be ascribed to the $^3H_4 \rightarrow {}^3P_0$ transitions of YAM:Pr^{3+}. None of the lines belonging to the Pr^{3+}-doped Y_2O_3 (20 028 cm^{-1})[20] or YAP (20 416.8 cm^{-1})[16] are present in the absorption spectrum.

The laser energy was successively adjusted to 20 668, 20 725, 20 763, and 20 821 cm^{-1}. These energies have been slightly tuned with respect to those measured on the absorption spectrum in order to optimize the emission signals. Three distinct emission spectra are recorded for the three lower energies. We label the sites from where they originate: A, B, and C, respectively. The spectra obtained for $E_{exc} = 20\,821$ cm^{-1} were obviously a mixture of A, B, and C without any additional lines. We conclude that only three $^3H_4 \rightarrow {}^3P_0$ transitions are detected in the YAM:Pr^{3+} compound at 20 668 ± 3, 20 725 ± 3, and 20 763 ± 3 cm^{-1}. The crystal structure announces the presence of four sites. Therefore, we have to assume that two sites are excited at nearly the same energy and give rise to very similar absorption and excitation spectra. The spectral line at 20 762 cm^{-1} (C) in the absorption spectrum is about twice as strong as those of A and B; it might be assumed that C hides two sites. This is what we shall try to clarify as well as to select the spectral lines pertaining to each site. Three strong, isolated $^3P_0 \rightarrow {}^3H_5$ emission lines at 18 411, 18 482, and 18 599 cm^{-1} pertaining unambiguously to A, B, and C, respectively, were selected as observation wavelengths, and excitation spectra were monitored by the emission at these energies. The resulting excitation spectra are represented in Figure 3. The excitation spectrum A monitored at 18 411 cm^{-1} shows a $^3H_4 \rightarrow {}^3P_0$ absorption at 20 668 cm^{-1} (A), followed by a small hump at 20 735 cm^{-1}. The emission at 18 482 cm^{-1} is fed by the absorption at 20 725 cm^{-1} (B) and also by two massifs around 20 806 and 20 819 cm^{-1}. The emission at 18 599 cm^{-1} is due only partly to $^3H_4 \rightarrow {}^3P_0$ at 20 763 cm^{-1} (C) and also to an absorption in a broad massif around 20 815 cm^{-1}. Therefore, we suggest that the four humps observed at 20 735, 20 806 and 20 819, and 20 815 cm^{-1} in the excitation spectra of A, B, and C, respectively, are the lowest $^3H_4 \rightarrow {}^1I_6$ lines belonging to these sites. The very weak presence of A in C shows that there is very little energy transfer from one site to another until 20 800 cm^{-1}. The excitation spectra confirm the conclusions of the absorption spectrum concerning the location of $^3H_4 \rightarrow {}^3P_0$ sites. Above 20 800 cm^{-1}, energy migrates easily between the $^1I_6$ levels of B and C. The lifetimes of the $^3P_0 \rightarrow {}^3H_4$ lines for sites A, B, and C are equal to 5, 16.2, and 6.2 μs, respectively, and Figure 5 represents the decays of the emissions when the sites are excited inside the $^3P_0$ levels. The decay of B is rigorously exponential, and its lifetime is about three times that of A and C. Therefore, it is possible, by time-resolved emission, to distinguish the lines originating from site B on one hand and sites A and C on the other, but difficult to separate site A from C.

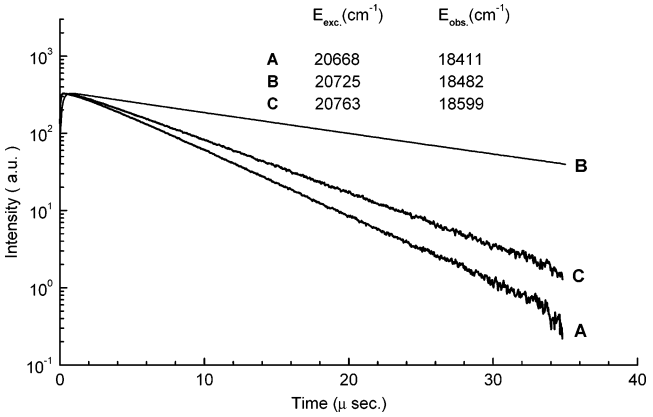

Figure 5. Decay of the $^3P_0$ emission in $Y_4Al_2O_9:Pr^{3+}$ (sample VI).

Emission Spectra of the Three Observed $^3P_0$ Levels

Emission spectra excited into the $^3P_0$ levels of A, B, and C and at 20 821 cm^{-1} (the spectra, labeled D, excited at 20 821 cm^{-1}, do not correspond to any additional site) are shown in Figures 6, 7, 8, and 9. They represent the $^3P_0 \rightarrow {}^3H_4$, $^3H_5$, $^3H_6 + {}^3F_2$, and $^3F_{3-4}$ spectral areas, respectively. Energy transfer between individual sites is weak at this temperature (20 K) and for this concentration. A is present in all spectra excited inside the $^3P_0$ levels, except in (B)$^3H_5$. Besides, the B spectra do not show up in the C spectra; the energy transfer between B and C is apparently nonexistent. The weak presence of site A in B might be due to the proximity of the $^3H_4 \rightarrow {}^1I_6$ and $^3H_4 \rightarrow {}^3P_0$ absorption energies of A and B. This explanation does not hold for the energy transfer of C toward A, because the (C)$^3P_0$ does not overlap any excitation energy of A. The presence of B together with C in the emission spectra excited at 20 821 cm^{-1} is understandable, because the excitation wavelength strikes into overlapping $^3H_4 \rightarrow {}^1I_6$ bands of B and C. From there, the energy migrates down toward A so that the three spectra are present on each figure.

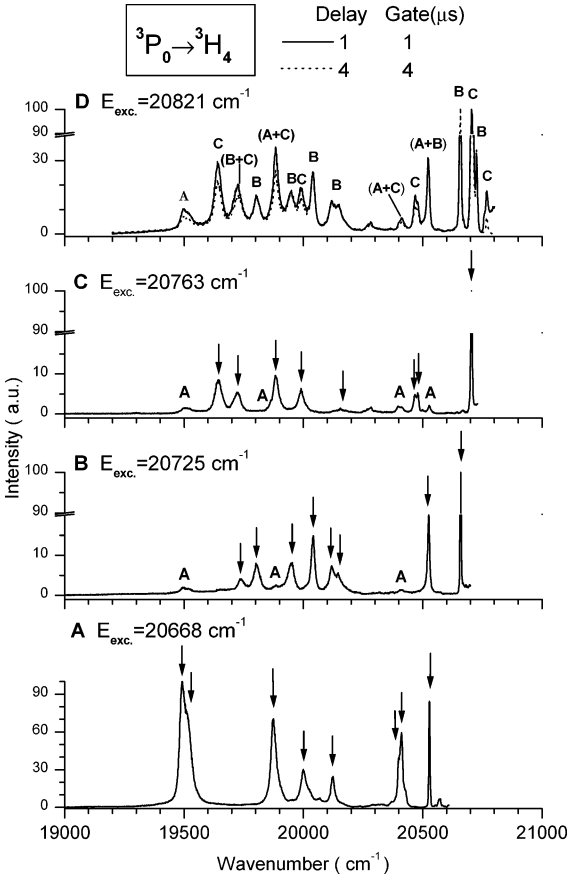

Figure 6. $^3P_0 \rightarrow {}^3H_4$ transitions at 20 K excited selectively in A, B, C, and D. The vertical arrows indicate which transitions are retained as belonging to the site.

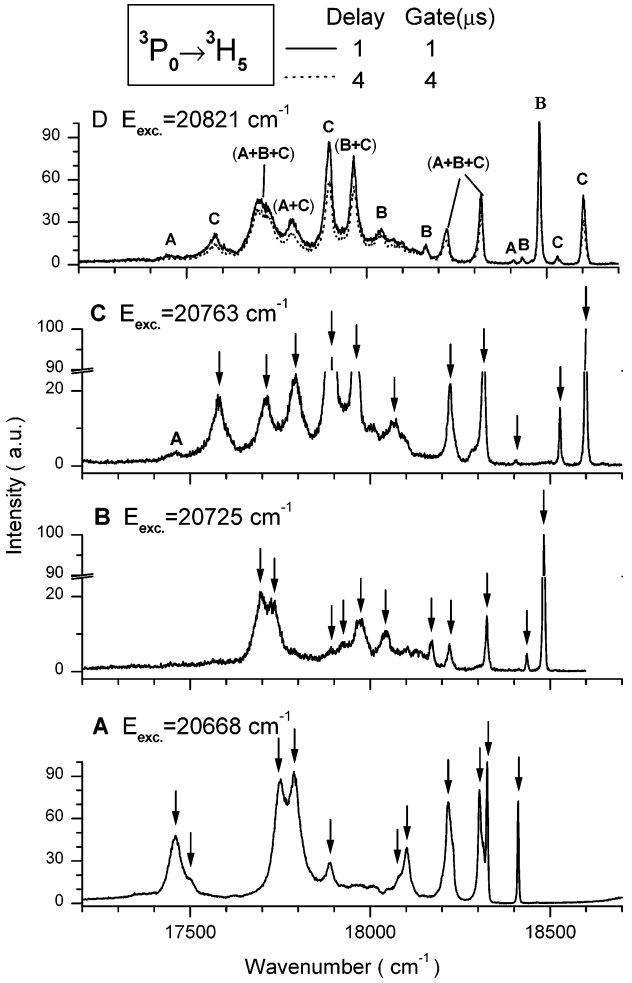

Figure 7. $^3P_0 \rightarrow {}^3H_5$ transitions at 20 K excited selectively in A, B, C, and D.

Table 2 lists the energies of the spectral lines recorded in the A, B, and C spectra. Optical spectroscopy shows evidence for only three sites. Once trimmed of spurious A lines, none of the three sets of spectra display much more than the ascribed number of lines. In particular, none of these spectra display twice as many lines as expected. Site C has less firmly identified lines than the other two. We admit that two sites are structurally so closely related that they give rise to nearly the same spectra. Coutures et al.[3] observed by low-temperature absorption three sites in $Nd_4Al_2O_9$ and $Nd_4Ga_2O_9$ obtained by splat cooling from the liquid state. Liu and Su[8] detected only two luminescent centers in $Y_4Al_2O_9$: Eu^{3+} and Tb^{3+}. The energy levels of each of the three sites deduced from the emission spectra (Figures 6−9) are listed in Table 3. The strongest lines measured in the absorption spectra as well as the correspondence with those deduced from the emission spectra are listed in Table 4. Some lines of the absorption spectrum are absent from the set found in the analysis of the emission spectra. The energies measured in emission are about 7 cm^{-1} higher than in absorption.

The $^3P_0 \rightarrow {}^3H_4$ transition of spectrum A in Figure 6 differs from that of B and C in that the high-energy lines are the strongest, while it is the opposite for B and C. The strong 19 493 cm^{-1} line belonging to A is visible in B and C. Likewise, in the $^3P_0 \rightarrow {}^3H_5$ spectral area, the high energy lines of the A spectrum are the strongest, and it is the other way around for B and C. The 17 459 cm^{-1} line of the A spectrum appears weakly in the C spectrum. Two sharp, unassigned shoulders appear at 18 314 and 18 230 cm^{-1} in the A spectrum. They might belong to C, although the $^3P_0$ level of C is higher than A in energy.

Nonradiative relaxation occurs between the $^3P_0$ and $^1D_2$ levels, so the 15 500−16 500 cm^{-1} spectral area is a complex one. It displays the $^3P_0 \rightarrow {}^3H_6$ lines of the A, B, and C sites. Two strong lines belonging to A, at 16 312 and 16 324 cm^{-1}, appear weakly in the B and C spectra, with lifetimes characteristic of the A site. In that area, the $^1D_2 \rightarrow {}^3H_4$ lines of the three sites and of the perovskite YAP:Pr^{3+} are observed as well. The emission of the latter occurs because of the relative positions of the four $^1D_2$ energy levels, which will be discussed later. The energies of the $^1D_2$ (1) $\rightarrow {}^3H_4$ (1−9) transitions in YAP:Pr^{3+}, deduced from the levels reported by Malinowski et al.,[16] are equal to 16 380, 16 328, 16 236, 16 228, 16 195, 16 151, 15 912, 15 856, and 15 740 cm^{-1}. The $^1D_2$ (1) $\rightarrow {}^3H_4$ lines, characterized by their long lifetimes, are easily detected. They can be separated into two groups with lifetimes approximately equal to 180 and 260 μs, respectively. The longer lifetimes pertain to the B site and the shorter ones to A and C. Their energies and tentative assignments are reported in Table 5. Four lines and one broad massif observed in the A spectrum are identified as $^1D_2$ (1) $\rightarrow {}^3H_4$ (1, 2, 4, 6, 8, 9) transitions of site A. The sequence of $^3H_4$ levels is then globally in agreement with the energies deduced from the $^3P_0 \rightarrow {}^3H_4$ (A) spectrum, which places the $^1D_2$ (1) (A) at 16 479 cm^{-1}. Sequences originating from the (B) $^1D_2$ (1) level are detected in the A, B, C, and D spectra. Transitions at 16 464 and 16 401 cm^{-1} with long lifetimes are, without ambiguity, assigned to (B) $^1D_2$ (1) $\rightarrow {}^3H_4$ (1, 2) respectively, which places the (B) $^1D_2$ (1) level at 16 464 cm^{-1}. These two assignments are confirmed in the four

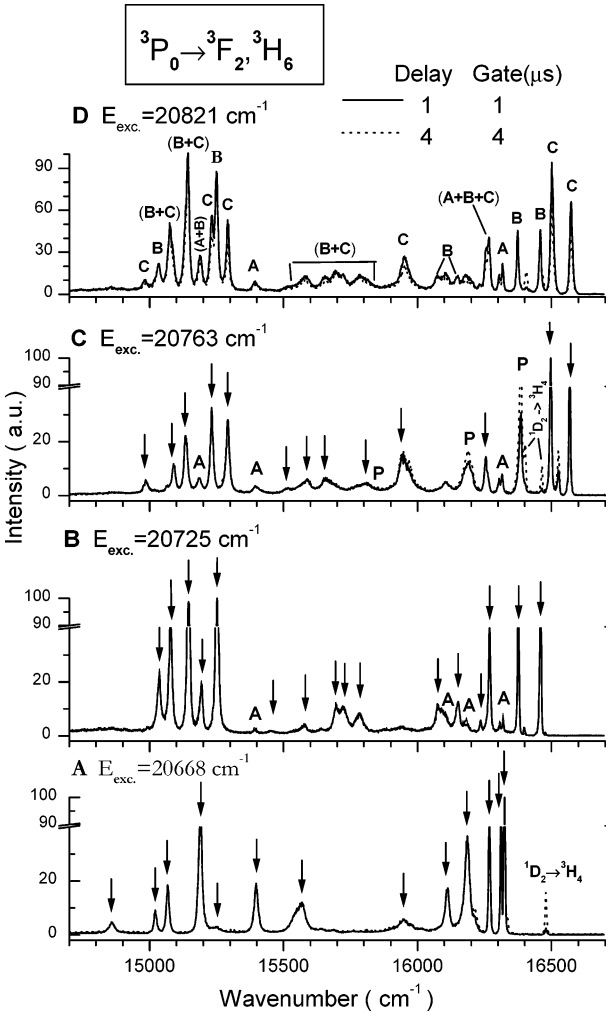

Figure 8. $^3P_0 \rightarrow {}^3H_6$, $^3F_2$ transitions at 20 K excited selectively in A, B, C, and D.

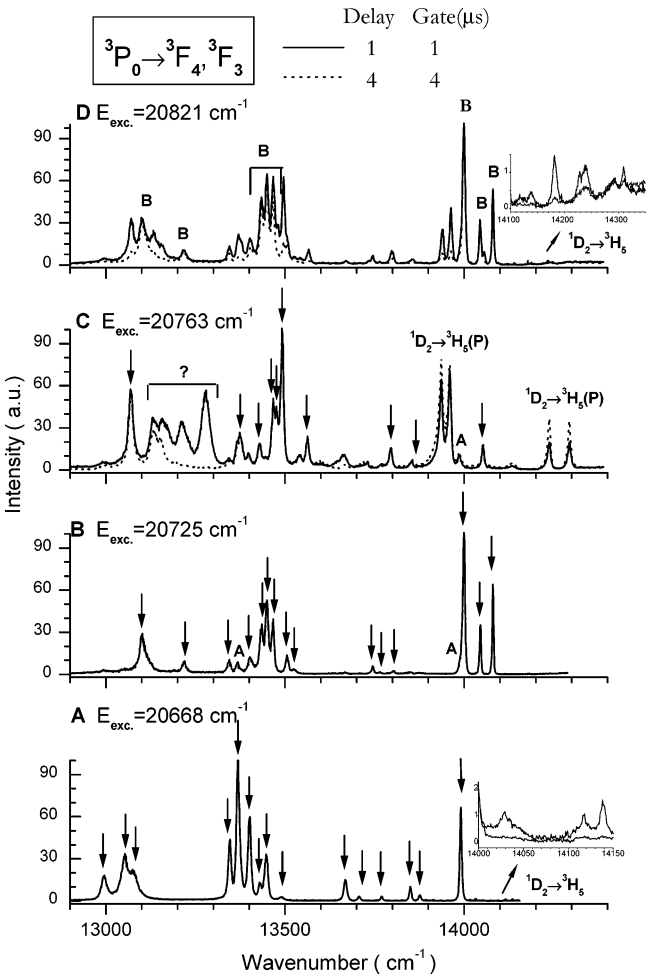

Figure 9. $^3P_0 \rightarrow {}^3F_3$, $^3F_4$ transitions at 20 K excited selectively in A, B, C, and D.

spectra. Spectrum C displays eight lines of mixed origin, among which two (at 16 385 and 16 189 cm^{-1}) are assigned to the perovskite[15] despite a very moderate agreement. But, no line can be assigned to the $^1D_2$ (1) $\rightarrow$ $^3H_4$ transitions of the C site. Besides, four lines with long lifetimes remain unassigned at 16 526, 16 199, 15 967, and 15 840 cm^{-1}. Within the 14 900−15 300 cm^{-1} zone, only the $^3P_0 \rightarrow {}^3F_2$ transitions are displayed.

The $^3P_0 \rightarrow {}^3F_{3,4}$ area extends from 12 900 to 14 200 cm^{-1}. Between 13 000 and 13 300 cm^{-1}, spectrum C is blurred by unassigned spurious lines with short lifetimes. Between 13 500 and 14 200 cm^{-1}, $^3P_0 \rightarrow {}^3F_3$ lines are superimposed with $^1D_2 \rightarrow {}^3H_5$ transitions. The latter are listed in Table 5. Spectrum A displays four lines, all of which belong to A. The A lines are also visible in C. Sharp lines assigned to YAP:Pr^{3+} are present in the C spectrum at 14 237, 13 960, and 13 936 cm^{-1}, as well as a small massif at 14 127−14 140 cm^{-1}. These energies agree with the values reported for $^1D_2$ (1) and $^3H_5$.[16] Spectrum D displays eight lines, all of which are assigned. Lines at 14 138, 14 028, and 13 917 cm^{-1} confirm the energies of (A) $^1D_2$ (1) $\rightarrow$ $^3H_5$ (2, 4, 5). The energies at 14 228 and 14 181 cm^{-1} are those of the (B) $^1D_2 \rightarrow {}^3H_5$ (1, 2) transitions, and the energies at 14 310, 14 239, 14 117, and 14 028 cm^{-1} match the sequence of (C) $^1D_2 \rightarrow {}^3H_5$ (1, 2, 3, 4) levels, which places the (C) $^1D_2$ (1) level at 16 474 cm^{-1}. The transitions observed in the other spectra confirm these assignments, except for spectrum C in which two lines remain unassigned. Energies 16 398, 16 401, and 16 406 cm^{-1} measured in spectra B, C, and D, respectively, correspond to the $^1D_2$ (1) $\rightarrow$ $^3H_4$ (2) energy of site B. We ascribe the differences between those measured values to the width of the absorption lines (7−20 cm^{-1} depending on the spectral area), which induces a shift of the emission if the excitation does not hit exactly at the center of the absorption line. The positions of the three lowest $^1D_2$ (1) levels are therefore determined at 16 479 (A), 16 464 (B), and 16 474 (C) cm^{-1} with an uncertainty of ±4 cm^{-1}. The insert in Figure 2b shows the 16 300−16 600 cm^{-1} part of the absorption spectrum recorded at 90 K. Two hot lines are visible at 16 341 and 16 414 cm^{-1}. The energy differences with respect to the strong lines originating from the ground state are equal to 140 and 61 cm^{-1}, respectively, which confirms that the lowest $^1D_2$ levels are located in the 16 465−16 480 cm^{-1} spectral range. We do not expect a closer agreement, given the width of the absorption lines.

One might suspect that the fourth Pr^{3+} site, which was not detected in the transitions from $^3P_0$, is responsible for the large number of unassigned lines in spectrum C. Then, the lowest $^1D_2$ (1) level of this site might be the unassigned feature, at 16 526 cm^{-1} (Table 5).

Our next goal is to proceed to a crystal-field analysis of each of the three energy level sequences listed in Table 3. With crystal structure and crystal-field parameters (CFPs) being closely connected, starting values will be deduced from the structure, refined by reference to the optical spectra, and the final values will be compared with the initial values for further identification. A good match with initial values will be considered a reliable matching test. Before proceeding to the evaluation of starting values, the crystal structure is examined in detail.

TABLE 2: Energies of the Spectral Lines (*E*'s) Observed in the Emission Spectra of $Y_4Al_2O_9:Pr^{3+}$ When Exciting Selectively in the $^3P_0$ Levels at 20 668 (A), 20 725 (B), and 20 763 (C) cm^{-1} [a]

A		B		C	
E	Δ*E*	*E*	Δ*E*	*E*	Δ*E*
		$^3P_0 \rightarrow {}^3H_4$			
20668	0	20725	0	20763	0
20571[b]	97	20659	66	20705	58
20528	140	20525	200	20668[b]	95
20411	257	20145	580	20479	284
20399 sh[b]	(269)	20119	606	20467	296
20123	545	20041	684	20150	613
20001	667	19950	775	19991	772
19874	794	19805	920	19885	878
19511 sh	(1157)	19739	986	19725	1038
19493	1175			19644	1119
		$^3P_0 \rightarrow {}^3H_5$			
18411	2257	18482	2243	18599	2164
18325	2343	18435	2290	18527	2236
18314 sh[b]	(2354)	18324	2401	18405	(2358)
18304	2364	18220	2505	18316	2447
18230 sh[b]	(2438)	18170	2555	18222	2541
18217	2451	18130[c]	(2595)	18066	2697
18102	2566	18099[c]	(2626)	18005[b]	2758
18081 sh	(2587)	18043	2682	17960	2803
17888	2780	17971	2754	17894	2869
17788	2880	17925	(2800)	17792	2971
17751	2917	17893	(2832)	17711	3052
17500 sh	(3168)	17728	2997	17580	3183
17459	3209	17698	3027		
		$^3P_0 \rightarrow {}^3H_6, {}^3F_2$			
16324	4344	16459	4267	16568	4195
16312	4356	16376	4349	16497	4266
16268	4400	16269	4456	16254	4509
16186	4482	16235	4490	16105[b]	4658
16111	4557	16151	4574	15946	4817
15948	4720	16078	4647	15805	4958
15567	5101	15940 vw[b]	(4785)	15659	5104
15398	5270	15880 vw[b]	(4845)	15587	5176
15248	(5420)	15783	4942	15515	5248
15190	5478	15721	5004	15292	5471
15068	5600	15695	5029	15232	5531
15021	5647	15641 vw[b]	(5084)	15135	5628
14859	5809	15577	5148	15090	5673
		15452 vw	(5273)	14987	5776
		15251	5474		
		15194	5531		
		15145	5580		
		15079	5646		
		15036	5689		
		$^3P_0 \rightarrow {}^3F_3, {}^3F_4$			
13990	6678	14080	6645	14053	6710
13876	6792	14045	6680	13854	6909
13850	6818	13999	6726	13795	6968
13770	6898	13803	6922	13563	7200
13707	6961	13764	6961	13540[b]	7223
13668	7000	13745	6980	13492	7271
13489	7179	13525	7200	13476	7287
13448	7220	13506	7219	13429	7334
13430	7238	13466	7259	13374	7389
13401	7267	13449	7276	13070	7693
13369	7300	13434	7291		
13346	7322	13403	7322		
13076	7592	13344	7381		
13053	7615	13218	7507		
12995	7673	13100	7625		

[a] Columns under Δ*E* list the 4f ^{2} levels. The emissions from $^1D_2$ are reported in Table 4. The values between parentheses are uncertain. All energies are in cm^{-1}. [b] Nonassigned. [c] Blurred, nonassigned.

TABLE 3: Experimental and Calculated Energy Levels

	spectrum A			spectrum B			spectrum C		
	exptl *E*	calcd *E*	Δ*E*	exptl *E*	calcd *E*	Δ*E*	exptl *E*	calcd *E*	Δ*E*
				$^3H_4$					
1	0	11	−11	0	−7	7	0	−4	4
2	140	145	−5	66	66	0	8	73	−15
3	257	258	−1	200	211	−11	284	277	7
4	−	465	−	580	579	1	296	301	−5
5	545	552	−7	606	624	−18	613	601	12
6	667	653	14	684	681	3	772	739	33
7	794	794	0	775	743	32	878	907	−29
8	1157	1139	18	920	921	−1	1038	1026	12
9	1175	1180	−5	986	984	2	1119	1120	−1
				$^3H_5$					
10	2257	2261	−4	2243	2245	−2	2164	2181	−17
11	2343	2331	12	2290	2298	−8	2236	2251	−15
12	2364	2366	−2	2401	2415	−14	2358	2370	−12
13	2451	2460	−9	2505	2526	−21	2447	2433	14
14	2566	2557	9	2555	2560	−5	2541	2590	−49
15	2587	2599	−12	2682	2663	19	2697	2699	−2
16	2780	2781	−1	2754	2763	−9	2803	2779	24
17	2880	2866	14	2800	2806	−6	2869	2867	2
18	2917	2919	−2	2832	2850	−18	2971	2973	−2
19	3168	3183	−15	2997	2985	12	3052	3066	−14
20	3209	3215	−6	3027	3005	22	3183	3147	36
				$^3H_6$					
21	4344	4320	24	4267	4264	3	4195	4174	21
22	4356	4359	−3	4349	4350	−1	4266	4241	25
23	4400	4412	−12	4456	4443	13	−	4493	−
24	4482	4470	12	4490	4471	19	4509	4514	−5
25	4557	4550	7	4574	4561	13	−	4730	−
26	4720	4737	−17	4647	4650	−3	−	4823	−
27	−	4785	−	−	4756	−	4817	4823	−6
28	−	4956	−	−	4921	−	−	4889	−
29	−	5011	−	4942	4954	−12	4958	4960	−2
30	5101	5094	7	5004	5021	−17	−	5092	−
31	−	5127	−	5029	5050	−21	5104	5107	−3
32	5270	5285	−15	5148	5140	8	5176	5197	−21
33	5420	5410	10	5273	5258	15	5248	5246	2
				$^3F_2$					
34	−	5437	−	5474	5493	−19	5471	5484	−13
35	5478	5464	14	5531	5521	10	5531	5528	3
36	5600	5586	14	5580	5555	25	5628	5613	15
37	5647	5641	6	5646	5641	5	5673	5698	−25
38	5809	5812	−3	5689	5714	−25	5776	5760	16
				$^3F_3 + {}^3F_4$					
39	6678	6662	16	6645	6637	8	−	6603	−
40	6792	6801	−9	6680	6687	−7	6710	6706	4
41	6818	6845	−27	6726	6742	−16	−	6822	−
42	6898	6887	11	6922	6902	20	6909	6895	14
43	6961	6962	−1	6961	6976	−15	6968	6980	−12
44	7000	7005	−5	6980	6980	−	−	7055	−
45	−	7093	−	7200	7186	14	7200	7185	15
46	7179	7177	2	7219	7205	14	7271	7261	10
47	7220	7225	−5	7259	7248	11	7287	7285	2
48	7238	7241	−3	7276	7259	17	7296	7297	−1
49	7267	7266	1	7291	7297	−6	7334	7339	−5
50	7300	7303	−3	7322	7336	−14	7389	7393	−4
51	7322	7323	−1	7381	7392	−11	−	7471	−
52	7592	7597	−5	7507	7508	−1	−	7613	−
53	7615	7612	3	−	7547	−	−	7667	−
54	7673	7673	0	7625	7635	−10	7693	7708	−15
64	16479[a]	−	−	16464[a]	−	−	16474[a]	−	−
				$^3P_0$					
69	20668	20671	−4	20725	20727	−2	20763	20763	0
				$^1I_6$					
70	20735	20740	1	20806	20805	1	20816	28017	−1
71	−	20751	−	20819	20823	−4	−	20839	−

[a] Not used for the fitting.

TABLE 4: Correspondence Between the Lines Observed in the Absorption Spectrum and the Energies Deduced from the Emission Spectra (Table 3)

3H4↓	absorption	assignment (emission)	3H4↓	absorption	assignment (emission)
$^3H_6$	4192	C (4195)	$^3F_3-^3F_4$	6644	B (6645)
	4262	B, C (4267, 4266)		6678	A, B(6678, 6680)
	4317			6707	C (6710)
	4338	A (4344)		6749	
	4392	A (4400)		6801	A (6792)
	4441	B (4456)		6817	A (6818)
	4478	A (4482)		6862	
	4496	C (4509)		6903	A, C (6898, 6909)
	4551	A (4557)		6960	A, B (6961, 6961)
	4936	B (4942)		6992	A (7000)
	4986			7270	A, B, C (7267, 7267,7271)
	5012	A (5011)		7294	A, B, C (7300, 7291,7296)
	5263	A (5270)		7320	A, B (7322, 7322)
	5372			7384	B, C (7381, 7389)
$^3F_2$	5465	C (5471)		7506	B (7507)
	5489			7532	
	5524	B, C (5531, 5531)		7616	A (7615)
	5574	B (5580)		7672	A (7673)
	5599	A (5600)		7713	
	5621	C (5628)		7745	
	5640	A, B (5647, 5646)			
	5675−80	B?, C (5689, 5673)			
	5706				
	5779	C (5776)			
	5807	A (5809)			
	5916				

TABLE 5: Emissions from $^1D_2$ (1) Observed When Exciting into $^3P_0$ (A, B, C, D)[a]

observed in	spectrum		
$^3P_0 \rightarrow {}^3H_6$	A	$^1D_2 \rightarrow {}^3H_4$	16 479 (A), 16 398 (B), 16 336 (A), 16 214 (A), 15 814 (A), 15 304−15 322 (A)
	B	$^1D_2 \rightarrow {}^3H_4$	16 477 (A), 16 464 (B), 16 398 (B)
	C	$^1D_2 \rightarrow {}^3H_4$	16 526 (?),16 464 (B), 16 401 (B), 16 385 (P), 16 199 (?), 16 189 (P), 15 967 (?), 15 840 (?)
	D	$^1D_2 \rightarrow {}^3H_4$	16 469 (B), 16 406 (B)
$^3P_0 \rightarrow {}^3F_3$	A	$^1D_2 \rightarrow {}^3H_5$	14 138 (A), 14 116 (A), 14 029 (A), 13 914 (A)
	C	$^1D_2 \rightarrow {}^3H_5$	14 293 (?), 14 237 (P), 14 127−14 140 (P,A), 14 027 (P,A), 13 960 (P), 13 936 (P), 13 728 (?), 13 601 (A)
	D	$^1D_2 \rightarrow {}^3H_5$	14 310 (C), 14 239 (C), 14 228 (B), 14 181 (B), 14 138 (A), 14 117 (C), 14 028 (A,C), 13 917 (A)

[a] P denotes YAP:Pr^{3+} lines.

The Crystal Structure of $Y_4Al_2O_9$

The cell of $Y_4Al_2O_9$ is monoclinic: $\vec{a}$ is perpendicular to $\vec{b}$, and the $(\vec{c},\vec{a})$ angle is equal to 108.58°. The structure contains four yttrium sites designated by Y(1), Y(2), Y(3), and Y(4). Their site symmetry is C_1, that is, without any symmetry element other than identity. The theoretical number of CFPs in C_1 is equal to 26 + 1 (one of them can be canceled), which is unwieldy. A first step consists of finding a pseudosymmetry element at the yttrium sites which would allow cancellation of some of the CFPs. Figure 10a shows the structure projected on the $(\vec{a},\vec{b})$ plane with $\vec{c}$ pointing obliquely out of the figure. It is viewed along $\vec{Ou}$, perpendicular to the figure plane. The structure is composed of roughly planar layers of oxygens sandwiching yttrium layers. The aluminum atoms are nested in roughly planar layers, every two oxygen layers. Figure 10b shows a slice of the structure consisting of two oxygen, one

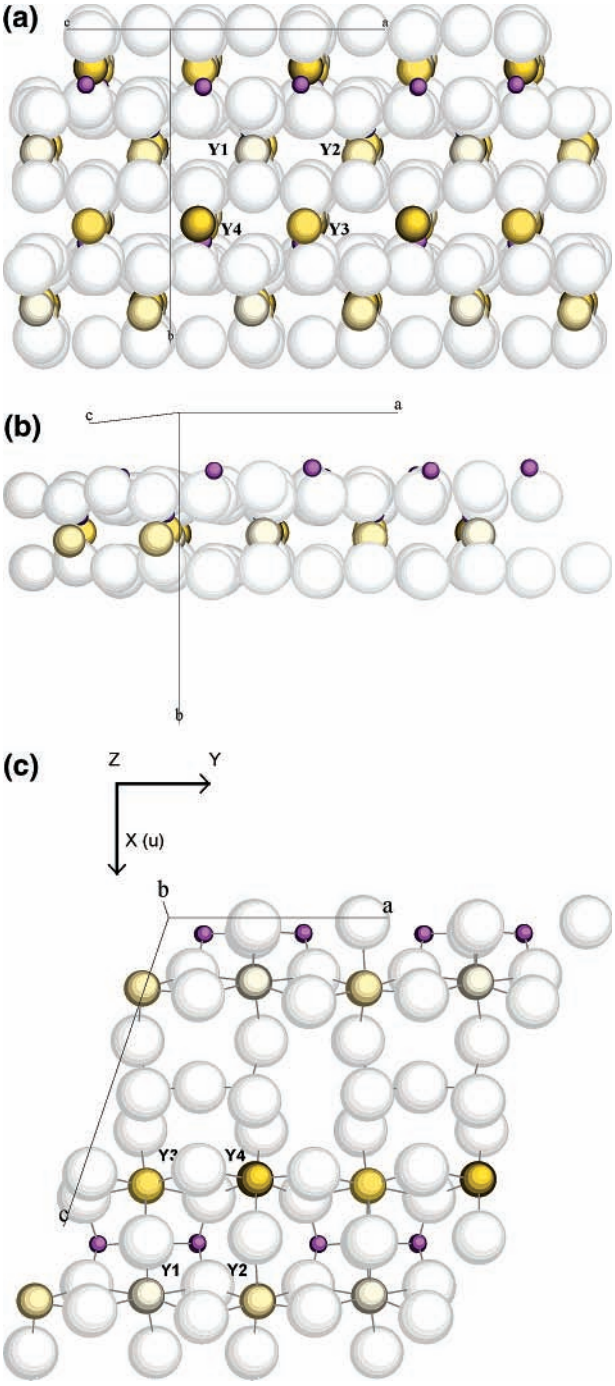

Figure 10. 10 (a). The structure of $Y_4Al_2O_9$ projected on the $(\vec{a}, \vec{b})$ plane with $\vec{c}$ pointing obliquely out of the figure.[21] (b) A slice of the structure consisting of two oxygen, one yttrium, and one aluminum layer. (c) The slice in part b has been rotated by 90° around $\vec{a}$. The adjacent coordination polyhedra of Y(1), Y(2), Y(3), and Y(4) are shown. The oxygens are represented by large open circles, the aluminums by small solid circles, and the yttrium by medium-size circles with progressively deeper shades along the sequence: Y(1), Y(2), Y(3), Y(4).

TABLE 6: Cartesian Coordinates and Distance (in Å) of the Closest Neighbors to Y(1), Y(2), Y(3), and Y(4)

site	ligand	*x*	*y*	*z*	*R*
Y(1)	O(1)	−0.2813	2.0036	1.3344	2.4237
	O(2)	−0.3372	−2.0206	1.3501	2.4535
	O(3)	0.7044	1.8261	−1.3134	2.3571
	O(5)	−1.7752	−0.0312	1.6464	2.4214
	O(6)	1.9379	0.2347	1.3071	2.3492
	O(7)	0.4606	−1.8303	−1.3586	2.3254
	O(9)	−1.8263	0.0366	−1.1495	2.1583
	Al(1)	−1.7283	−1.6754	2.2012	3.2618
	Al(2)	−1.7448	1.6773	2.2769	3.3229
Y(2)	O(1)	0.5854	1.6700	1.4350	2.2783
	O(2)	0.5879	−1.6806	1.4506	2.2966
	O(3)	−0.5376	1.8475	−1.1576	2.2455
	O(4)	−1.6591	0.2028	1.5442	2.2756
	O(7)	−0.3505	−1.8709	−1.2126	2.2569
	O(8)	2.1070	0.0563	−1.1068	2.3806
Y(3)	O(2)	−1.8929	−0.1352	1.4269	2.3743
	O(4)	0.2889	−2.0959	1.4510	2.5655
	O(5)	1.9267	−0.0882	1.4311	2.4017
	O(6)	0.4594	2.0393	1.4699	2.5555
	O(8)	−0.4651	−1.7990	−1.3523	2.2981
	O(9)	−0.4476	1.7832	−1.3270	2.2674
	O(9)	1.8780	−0.0185	−1.3649	2.3217
	O(3)	−3.0393	0.0832	−1.1631	3.2553
	Al(1)	−3.2712	0.2583	0.5758	3.3315
	Al(1)	1.9163	−1.7330	1.9858	3.2586
	Al(2)	2.0168	1.6182	2.0615	3.3069
Y(4)	O(1)	−1.6566	0.1043	1.5162	2.2481
	O(4)	0.5244	1.6681	1.5246	2.3199
	O(6)	0.6377	−1.5661	1.5435	2.2895
	O(8)	−0.2505	1.9049	−1.2787	2.3079
	O(8)	1.9497	0.0662	−1.2661	2.3257
	O(9)	−0.2464	−1.8926	−1.2535	2.2834
	O(7)	−2.6126	−0.1272	−1.0444	2.8165
	Al(1)	−3.1044	−0.2856	0.5737	3.1699

yttrium, and one aluminum layer. Figure 10c represents the same slice rotated by 90° around $\vec{a}$ in order to display the adjacent coordination polyhedra of Y(1), Y(2), Y(3), and Y(4). The view is along $\vec{b}$. The four nonequivalent yttrium ions occupy the corners of a distorted square, in the counterclockwise order: 1−2−4−3. This quasiplanar association of four yttrium atoms repeats itself throughout the structure. Y(1) and Y(2) atoms, on one hand, and Y(3) and Y(4) on the other run on linear chains parallel to $\vec{a}$. The ($\vec{b}$,$\vec{Ou}$) plane, perpendicular to Figure 10c, is a pseudosymmetry plane for the four yttrium sites and might be the pseudosymmetry element we are searching for. To check that assumption, a point-charge calculation was carried out in a Cartesian system *XYZ* centered on yttrium, in which *OX*, *OY*, and *OZ* are along $\vec{Ou}$,$\vec{a}$, and $\vec{b}$, respectively (*XOZ* is the symmetry plane). In that system, the imaginary parts of nearly all of the calculated CFPs cancel. The total number of CFP parameters is reduced to 14 + 1 ($k = 2$, 4, 6, and $q = 0 \rightarrow k$). One parameter can be arbitrarily set equal to 0. To display a true C_s site symmetry, *Z* and *Y* are interchanged (a 90° rotation); then, only the B_q^k's with even *q*'s are nonvanishing, but the imaginary components S_q^k's are allowed as well. On a whole, the number of parameters to be fitted is the same (14 + 1) as before. The two procedures are equivalent and give exactly the same energies when introduced in the interaction matrix. Actually, it is easier to utilize the first coordinate system, in which all of the B_q^k's are nonvanishing and mostly real. The coordinates of the nearest neighbors and closest next-nearest neighbors with respect to the yttrium ions at distances lower than 3.4 Å are listed for the four sites in Table 6. For all pairs of neighbors, when *y* is nonzero, the *y* values are opposite, while *x* and *z* are very close. For a true symmetry plane, these conditions would be respected exactly. Figure 10c shows the coordination polyhedra and their linkages. Y(1) has seven oxygen neighbors at a mean distance equal to 2.355 Å, including one at a very short distance (2.158 Å), which is difficult for the large doping ion to withstand. Two aluminum ions are at 3.3 Å. The coordination polyhedron of Y(2) is more isolated. Y(2) has six oxygen neighbors at a mean distance equal to 2.289 Å. The two nearest aluminum atoms do not appear before 3.6 Å. Y(3) resembles Y(1); it also has seven nearest oxygen neighbors (at a mean distance 2.398 Å) and two aluminum atoms at 3.3 Å, but in addition, it has one more oxygen and one aluminum at 3.3 Å in the pseudosymmetry plane. On a whole, it has 11 close neighbors or next-nearest neighbors, seven of which are in the pseudosymmetry plane and, hence, are hidden by other ions in Figure 10c. The common feature Y(4) shares with Y(2) is the presence of six close oxygen neighbors (at a mean distance of 2.296 Å), but Y(4) has additional Al and O atoms at 2.817 and 3.170 Å, respectively.

TABLE 7: Predicted Crystal-Field Parameters (cm^{-1}) for $Y_4Al_2O_9:Pr^{3+}$

	Y(1)		Y(2)		Y(3)		Y(4)	
k, *q*	B_q^k	S_q^k	B_q^k	S_q^k	B_q^k	S_q^k	B_q^k	S_q^k
2, 0	−99	0	9	0	210	0	766	0
2, 1	−370	203	−940	−196	−298	137	−1276	−63
2, 2	−191	345	−1361	293	−334	−93	−1206	132
4, 0	−2248	0	−2295	0	−2162	0	−2524	0
4, 1	417	5	235	−31	13	−24	137	52
4, 2	3	−99	−852	141	−27	−19	−549	141
4, 3	−1630	−120	−2188	−93	−1157	24	−2059	75
4, 4	1049	−4	1006	−4	942	2	936	−3
6, 0	934	0	765	0	800	0	551	0
6, 1	3	−65	−6	74	71	−26	230	−3
6, 2	192	98	368	−69	44	17	276	14
6, 3	−35	−44	−425	−55	345	−27	−813	−20
6, 4	1388	−49	1130	97	1395	26	1312	−6
6, 5	147	233	506	−182	437	151	314	−143
6, 6	233	−35	166	78	195	0	56	−23

Starting Crystal-Field Parameters at the Four Yttrium Sites: The Covalo-Electrostatic Model

The covalo-electrostatic model[22] was utilized to obtain starting sets of CFPs from the $Y_4Al_2O_9$ structure. In that model, the interactions contributing to the splitting of the electronic levels are electrostatic and covalent interactions. The model takes into account the next-nearest neighbors of the central ion and was applied to several classes of compounds.[23] The covalent contribution is assumed to be mainly kinetic energy with ionization energies equal to −85 000, 0, and −120 000 cm^{-1} for Pr^{3+}, Al^{3+}, and O^{2-}, respectively. For $k = 2$ and 4 parameters, one-fourth of the point-charge electrostatic interaction evaluated with usual ionic charges is added. The yttrium positions determined by the single-crystal neutron refinement of $Y_4Al_2O_9$[5] are utilized. The results (calculated parameters of the four sites) are listed in Table 7. The imaginary components of the largest parameters are much smaller than the real components, which confirms the assumption made of a pseudosymmetry plane. It is noteworthy that B_0^4, B_3^4, B_4^4, B_0^6, and B_4^6 are large for the four sites, and B_3^6 is large in site 4. Grossly, the symmetry can be considered as the superposition of 4-fold and 3-fold symmetry having the same axis.

Crystal-Field Analysis of Spectra A, B, and C

The energy level schemes of the three experimental spectra A, B, and C were simulated by determining the parameters of

the standard one-electron Hamiltonian on the basis of the 91 basis states of the $4f^2$ configuration of Pr^{3+}:

$$\mathbf{H} = \sum F^k \cdot \mathbf{f}_k + \zeta \cdot A_{so} + \alpha L(L+1) + \beta G(G_2) + \gamma G(R_7) + \sum_k M^k \cdot m_k + \sum_k P^k \cdot p_k + \sum_{kq} B^k_q \cdot C^k_q$$

It includes the usual interactions: the electrostatic two-electron repulsion (parameters: F^2, F^4, F^6), the free-ion interconfiguration interaction (parameters: α, β, γ), the magnetic interaction (parameters: M^k, P^k), the spin−orbit interaction (parameter: ζ), and the crystal-field interaction (parameter: B^k_q).[24,25] Refinements of the Hamiltonian parameters were carried out, utilizing the starting sets of the CFPs listed in Table 7. The imaginary components of the CFPs are small. Except for S^2_1 and S^2_2 in sites A and B, they were not considered, and the refinements utilized 14 + 1 real CFPs.

The total number of electronic energy levels in the $^3H_{4\rightarrow6}$, $^3F_{2\rightarrow4}$ manifolds is equal to 54. Data sets A, B, and C include 47, 51, and 43 of these levels, respectively. Only two $^3H_6$ and one $^3F_4$ levels are missing in data set B. To the A and C lists are added $^3P_0$ and the lowest $^1I_6$ level, which makes totals of 49 and 45 for A and C, respectively. For spectrum B, $^3P_0$ and two $^1I_6$ levels are introduced, hence a total of 54 levels. These levels are useful to stabilize the free-ion parameters. We tried without success to fit the spectra with all the spherically symmetric parameters fixed. The goal could not be attained, and only F^2, F^4 and F^6 were fixed for the three spectra, while α, β, γ, M^0, and P^2 were allowed to vary. The refined values of the Hamiltonian parameters for spectra A, B, and C are reported in Table 8. The final mean deviations between experimental and fitted energy levels are equal to 10.1, 13.3, and 16.1 cm^{-1}, respectively. Spectra A and B are the best fitted. No imaginary $k = 2$ component was utilized for B because it did not improve significantly the experimental/calculated fit. In C, the lowest $^3H_5$ level is the most discrepant, calculated at 49 cm^{-1} from its experimental values, and two other levels are at more than 30 cm^{-1}. This confirms that some lines of the experimental C spectrum probably belong to another site, and that might be the reason for the unrealistic value of M^0 (C).

The next task is the comparison between fitted and predicted CFPs in order to assign each site to a particular spectrum. To compare two sets, the CFPs are considered as generalized vectors, and two quantities have been defined: a scale factor comparing the lengths of the experimental and calculated vectors and a reliability factor giving the angle between the experimental and calculated vectors.[24]

The scale factor is written as

$$s_k = |B^k_{exptl}|/|B^k_{calcd}|$$

with

$$|B^k| = \left[\sum B^k_q \cdot B^{k*}_q\right]^{1/2}$$

and the reliability factor as

$$r_k = \arccos\left[(B^k_{exptl} \cdot B^k_{calcd})/(|B^k_{exptl}| \cdot |B^k_{calcd}|)\right]$$

A complete agreement between experimental and calculated crystal-field parameters occurs if the generalized vectors are coincident, that is, when their lengths are equal ($s_k = 1$) and the angle between them is equal to zero ($r_k = 0$ deg). These quantities can be utilized to compare any two sets of parameters, either experimental or calculated. In the present case, the scale and reliability factors are evaluated between pairs of experimental and calculated parameters and listed in Table 9. It can be stated that the $k = 2$ scale factors vary wildly between 0.6 and 3. The $k = 2$ reliability factors are in most cases high (large

TABLE 8: Fitted Free-Ion and Crystal-Field Parameters for $Y_4Al_2O_9:Pr^{3+}$ [a,b]

	spectrum (A)	spectrum (B)	spectrum (C)
E_0	11735	11876	11927
ζ	754.3	757.1	721.5
α	19.87	17.89	19.20
β	−581	−524	−378
γ	1716	1808	1716
M^k	0.04	1.03	−3.87
P^k	−372	−390	465
B^2_0	359	225	399
B^2_1	−480	−565	66
S^2_1	191	0	0
B^2_2	−614	32	729
S^2_2	−50	0	0
B^4_0	−2745	−2849	−1724
B^4_1	−270	498	721
B^4_2	174	−331	−803
B^4_3	−1881	−816	−1731
B^4_4	658	1644	1416
B^6_0	957	805	1219
B^6_1	50	29	141
B^6_2	147	−100	−336
B^6_3	32	213	−190
B^6_4	1199	1703	1937
B^6_5	369	202	221
B^6_6	209	0	−276
N	49	54	45
n	24	22	22
σ[c]	10.1	13.3	16.1
SD[d]	14.1	17.3	22.5

[a] Values in cm^{-1}. [b] For the three calculations: $F^2 = 67270$, $F^4 = 47566$, $F^6 = 31460$ cm^{-1}; $M^2/M^0 = 0.56$, $M^4/M^0 = 0.31$; $P^4/P^2 = 0.75$, $P^6/P^2 = 0.5$. N and n stand for the number of levels and parameters allowed to vary freely, respectively. [c] σ = mean deviation (nonbary-centered). [d] SD = standard deviation: $[\sum_{i=1,N}(Ei_{exptl} - Ei_{calcd})^2/(N - n)]^{1/2}$.

TABLE 9: Scale and Reliability Factors for the CFPs of Experimental Spectra A, B, and C with Respect to the Calculated Spectra for Sites 1, 2, 3, and 4

		reliability factor r^k (deg)			scale factor s^k		
spectrum	site	2	4	6	2	4	6
A	1	52.5	19.3	14.3	0.69	0.91	1.10
A	2	29.9	25.0	23.6	2.01	1.09	1.03
A	3	9.0	15.9	16.7	0.59	0.76	1.12
A	4	18.7	18.3	34.6	2.20	1.05	1.15
B	1	55.9	24.5	19.4	0.99	0.91	0.88
B	2	60.6	33.1	35.8	2.9	1.09	0.82
B	3	52.0	20.4	23.9	0.85	0.77	0.89
B	4	44.8	30.6	40.2	3.14	1.05	0.92
C	1	113.7	21.7	24.8	0.74	0.92	0.73
C	2	142.5	17.0	35.0	2.16	1.10	0.68
C	3	124.3	27.7	22.3	0.64	0.77	0.74
C	4	124.1	20.8	34.1	2.35	1.06	0.76

angle between the experimental and calculated parameters). The best agreement occurs for the pair: spectrum A ↔ site 3 with r^2, r^4, and r^6 equal to 9.0°, 15.9°, and 16.7°, respectively. A match is more difficult to find for B. The smallest discrepancy connects spectrum B and site 1 with r^2, r^4, and r^6 equal to 55.9°, 24.5°, and 19.4°, respectively. No really satisfying match is found for C in Table 9. Considering an eventual correspondence between spectrum C and site 2, s^4 is acceptable, but the s^2 value seems prohibitive, with experimental and calculated values of the second-order parameters displaying nearly opposite values. An attempt to correct the calculated B^2's by adding electrostatic dipolar corrections leads to no improvement with respect to experimental values. Several points need to be considered: (a) the difference between the ionic radii of Y^{3+} and Pr^{3+} (the larger ion is likely to distort locally the structure, and the second-order CFPs are very sensitive to structural changes), (b) predicted second-order parameters should not be trusted too much, because they have led to erroneous interpretations as shown in ref 26, and (c) as pointed out here, two spectra are probably concealed in C.

It is noteworthy that reliability factors can be useful for the purpose of comparing any two environments on a quantitative basis. The polyhedra of the four crystallographic sites can be globally compared, considering scale and reliability factors of their calculated CFPs. Sites 1 and 3 have seven first neighbors, while sites 2 and 4 have six. At first glance, sites 1 and 3 and sites 2 and 4 look alike. When evaluated on a quantitative basis by scale and reliability factors, it is found for the site 1 ↔ site 3 pair that s^k values equal 0.86, 0.84, and 1.02 and r^k values equal 56.8°, 12.6°, and 17.4° for $k = 2, 4, 6$, respectively, which is modest evidence of resemblance. A similar comparison for the pair site 2 ↔ site 4 gives 1.09, 0.97, and 1.12 for s^k's and 21.8°, 8.0°, and 20.8° for r^k's, which are rather better values.

Energy Transfer between Sites

The energy transfer between the three sites is small. A is the lowest in energy. As pointed out already, B and C transfer weakly toward A, and there exists no detectable transfer between C and B, although C is at higher energy than B. The lowest $^1I_6$ level of A is nearly coincident with $^3P_0$ (B), which may be the reason for the weak excitation of A when the excitation is tuned at that energy. The Pr^{3+} concentration is equal to 0.5%. If no significant clustering occurs and the Pr^{3+} ions are randomly substituted in the Y^{3+} sites, the mean distance between any two Pr^{3+} ions is 21.7 Å, while the mean distance between equivalent Pr^{3+} ions is 34.4 Å (the proportions of Y(1), Y(2), Y(3), and Y(4) are assumed to be equal). These long distances explain the weakness of energy transfer between Pr^{3+} centers. If there were no preference for transfer from one site to another, then B lines would be excited when energy is tuned on the $^3P_0$ (C) energy. Blasse[27] notes that if the distance between the rare-earth ions is on the order of 4 Å, the effective transfer rate between Eu^{3+} or Gd^{3+} ions is 10^4 times larger than the radiative rate and hopping occurs along a very large distance during the lifetime of the excited state. Besides, Selzer and Yen[28] underline that radiative transfer is generally not observed in rare-earth crystals but becomes predominant at low concentrations. It is puzzling that two Pr^{3+} ions doped in two sites of the $Y_4Al_2O_9$ structure transfer toward a third one (the fourth site has not been observed in this work), while the former two do not transfer toward one another. If one assumes that energy from each site is transferred to an identical distant site by resonant radiative transfer, and then transferred to the nearest available neighbor, then some elements should be found in the structure to interpret the experimental observation. Table 10 indicates the number of yttrium ions surrounding a particular site within a sphere with a radius equal to 5 Å. One can assume that Pr^{3+} substituted to Y(1), which has no equivalent close neighbors, transfers less than the other sites. That would allow one to identify it as responsible for spectrum B. Y(1) has only two contacts with Y(2) and Y(4), which might lead to the assumption that one of these two sites gives rise to C, provided they are also occupied by a doping ion. This interpretation implies a certain degree of clustering. It has also been mentioned that spectra B and A are quite different. Hence, A might originate from Y(2) or Y(4). Two possibilities are therefore suggested: A → Y(2), B → Y(1), C → Y(4) or A → Y(4), B → Y(1), C → Y(2). A fourth site, C′, is likely to be concealed in C. The reliability factors for the pair A → Y(2) or A → Y(4) are not excellent but acceptable.

TABLE 10: Number of Yttrium Ions Surrounding a Particular Site within a Sphere 5 Å in Radius

	Y(1)	Y(2)	Y(3)	Y(4)
Y(1)	0	2	3	2
Y(2)	2	1	2	3
Y(3)	3	2	1	3
Y(4)	2	3	3	1

Conclusion

Synthesis conditions have been optimized in order to prepare the phase $Y_4Al_2O_9:Pr^{3+}$ with a satisfying degree of purity. Very small amounts of $YAlO_3:Pr^{3+}$ are present in the samples, however.

Spectroscopic investigations have been made on the samples in order to check the number of Pr^{3+} sites substituted to Y^{3+}. Under site-selective excitation of the $^3P_0$ levels at 20 K, three distinct emission spectra are obtained. That is not in agreement with the results of structural analyses, which have indicated the presence of four crystallographic sites for Y^{3+}. It is suggested that two sites are excited at the same $^3P_0$ energy and that a fourth spectrum is concealed in one of the experimentally observed spectra. The three energy level sets of $4f^2$ electronic levels have been analyzed by a conventional crystal-field analysis. It is found that one of the energy level sets is less well fitted than the other two, which seems to confirm the assumption made already. A tentative correlation is made between experimental spectra and crystallographic sites by considering the energy transfer between sites and the agreement between predicted and fitted crystal field parameters.

References and Notes

(1) Schneider, S. V.; Roth, R. S.; Waring, U. L. *J. Res. Natl. Bur. Stand.* **1961**, *A65*, 345.
(2) Brandle, C. D.; Steinfink, H. *Inorg. Chem.* **1969**, *8*, 1320.
(3) Coutures, J. P.; Antic, E.; Caro, P. *Mater. Res. Bull.* **1976**, *11*, 699.
(4) Dohrup, J.; Høywald, A.; Mogensen, G.; Jacobsen, C. J. H.; Villadsen, J. *J. Am. Ceram. Soc.* **1996**, *79*, 2959.
(5) Christensen, A. N.; Hazett, R. G. *Acta Chem. Scand.* **1991**, *45*, 226.
(6) Yamane, H.; Shimada, M.; Hunter, B. A. *J. Solid State Chem.* **1998**, *141*, 466.
(7) (a) Shimada, M.; Nomura, M.; Yamane, H. *Adv. Sci. Technol. (Faenza, Italy)* **1999**, C589−592. (b) Shimada, M.; Yamane, H.; Takizawa, H.; Endo, T. Phase transformation of $Gd_4Al_2O_9$ at high temperature. Presented at Euroceramics V, Versailles, France, June 22−26, 1997.
(8) Liu, S.; Su, Q. *J. Alloys Compd.* **1997**, *255*, 102.
(9) Moune, O. K.; Rabinovitch, Y.; Tétard, D.; Pham-Thi, M.; Lallier, E.; Faucher, M. D. *Eur. Phys. J. D* **2002**, *19*, 275.
(10) Yamane, H.; Omori, M.; Hirai, T. *J. Mater. Sci. Lett.* **1995**, *14*, 561.
(11) Papadopoulos, I. *Cryst. Res. Technol.* **1991**, *26*, 409.
(12) Harlan, C. J.; Kareiva, A.; MacQueen, D. B.; Cook, R.; Barron, R. *Adv. Mater. (Weinheim, Ger.)* **1997**, *9*, 68.

(13) Lo, J. R.; Tseung, T. Y. *Mater. Chem. Phys.* **1998**, *58*, 56.
(14) Rabinovitch, Y.; Tétard, D.; Faucher, M. D.; Pham-Thi, M. *Opt. Mater. (Amsterdam)* **2003**, *24*, 345.
(15) Rabinovitch, Y. Céramiques transparentes de YAG dopé terres rares: synthèse, caractérisation, mesures en cavité laser et études spectroscopiques. PhD Thesis, Ecole Centrale Paris, 2002.
(16) Malinovsky, M.; Garapon, C.; Joubert, M. F.; Jacquier, B. *J. Phys.: Condens. Matter* **1995**, *7*, 199.
(17) Toropov, N. A.; Bondar, I. A.; Galakhov, F. Y.; Nikogosyan, X. S.; Vinogradova, N. V. *Izv. Akad. Nauk SSSR, Ser. Khim.* **1964**, *7*, 1162.
(18) Goldschmidt, V. M. *Skr. Nor. Vidensk—Akad. [Kl] 1: Mat.—Naturvidensk. Kl.* **1926**, 8.
(19) Piriou, B.; Rager, H.; Schneider, H. *J. Eur. Ceram. Soc.* **1996**, *16*, 195.
(20) Leavitt, R. P.; Gruber, J. B.; Chang, N. C.; Morrison, C. A. *J. Chem. Phys.* **1982**, *76*, 4775.
(21) Boudias, C.; Monceau D. *CaRIne, Crystallography*, version 3.1; Senlis, France, 1989-1998.
(22) Garcia, D.; Faucher, M. *J. Chem. Phys.* **1985**, *82*, 5554.
(23) Faucher, M.; Garcia, D.; Moune, O. K. *J. Lumin.* **1992**, *51*, 341.
(24) Judd, B. R.; Crosswhite, H. *J. Opt. Soc. Am. B* **1984**, *1*, 255.
(25) Judd, B. R. *Operator Techniques in Atomic Spectroscopy*; Princeton University Press: Princeton, NJ, 1998.
(26) Tanner, P. A.; Wong, K. L. *J. Phys. Chem. B* **2004**, *108*, 136.
(27) Blasse, B.; Grabmaier, B. C. *Luminescent Materials*; Springer-Verlag: New York., 1994.
(28) Selzer, P. M.; Yen, W. M. *Opt. Lett.* **1977**, *1*, 90.